



ORIGINAL RESEARCH ARTICLE

Effect of Inter-pass Layer Temperatures on Microstructure and Mechanical Properties of Inconel 625 Fabricated Using Wire and Arc Additive Manufacturing

M. Karmuhilan  and Somasundaram Kumanan

Submitted: 26 July 2023 / Revised: 14 December 2023 / Accepted: 22 December 2023

A large amount of heat is involved in the wire and arc additive manufacturing (WAAM) process under high deposition rate conditions. Energy accumulation affects the properties of the parts being produced. This article discusses the effect of inter-pass layer temperature on the microstructural and mechanical characterization of Inconel 625. Three samples were additively manufactured for three different inter-pass layer temperatures (100, 200, and 300 °C) using the WAAM technique. The analysis shows that the grain morphology varies with different IPTs. Compared to the sample deposited with IPT 100 °C, the sample deposited with IPT 300 °C has less Cr, Nb, and Mo. Electron backscatter diffraction identified the grain size increased from 30.83 to 70.77 μm with increasing IPT. Grain boundary distribution angles also significantly varied with a change in IPTs. The variation in peak intensity identified the preferred crystal orientation through x-ray diffraction analysis. The decrease in inter-pass layer temperatures increased ultimate tensile strength by 7.3% and yield strength by 10.4%. The average microhardness values increased by 11.5% with a reduction of IPT.

Keywords inter-pass layer temperature, Inconel 625, mechanical properties, microstructure, wire and arc additive manufacturing

1. Introduction

Inconel 625 is a nickel-based superalloy with high tensile, corrosion resistance, and fatigue strength. It possesses superior strength at higher temperatures (Ref 1-4). It is employed in aeronautical parts like thrust reverser systems, hydraulic tubing, spray bars, turbine shrouds, and armoring. Additionally, it is utilized to remanufacture gas turbine items that have structural damage (Ref 5-7). This alloy exhibits poor machinability due to strain hardening and increased tool wear rate. Investigation of new methods needs attention for manufacturing complex shapes (Ref 8). Wire and arc additive manufacturing (WAAM) is a promising additive manufacturing (AM) method with low cost and high printing efficiency (Ref 9-12). Due to its high deposition rate and low feedstock, WAAM uses gas metal arc welding (GMAW) with robotic assistance (Ref 13). In GMAW, better tool path control can be achieved by feeding the wire via the torch. CMT (Cold Metal Transfer) melting technology performs well on the steady transfer model and heat input control (Ref 8, 14, 15).

Heat accumulation is an inevitable criterion that influences the geometrical accuracy, microstructural evaluation, and material properties in the WAAM process. Inter-pass layer temperature (IPT) determines heat accumulation (Ref 16). The crystalline phase, grain size, and microstructure varied in Ti6Al4V parts along the building direction due to thermal accumulation, which also changed the mechanical properties and fracture features. Maintaining the inter-pass temperature below 200 °C ensured the acceptable quality of Ti6Al4V parts (Ref 17). Montevecchi et al. performed the impingement of air jets on the deposited layer using an FE thermal model of the weld-based AM process. It prevented heat accumulation by keeping the average temperature and controlling the molten pool size (Ref 18). Wu et al. studied the influence of CO₂-forced cooling and IPT of WAAM Ti6Al4V parts. It was reported the importance of IPT on geometrical stability and surface oxidation (Ref 19). Using a finite element (FE) simulation model, Montevecchi et al. created an algorithm to calculate inter-layer idle time. This idle time maintained IPT and controlled the molten pool size to prevent a catastrophic collapse (Ref 20). Cuiuri et al. studied the impact of inter-pass layer temperature of additively manufactured γ -TiAl alloy by in situ monitoring. An increase in inter-pass layer temperature from 100 to 400 °C decreased the microhardness (Ref 21). The discussion shows that IPT is crucial in surface oxidation, mechanical properties, microstructural evaluation, and geometrical stability. WAAM-processed Inconel 625 parts maintained a constant IPT of 400 °C. The increased travel speed increased the hardness and tensile strength (Ref 22).

Shen et al. (Ref 23) reported the WAAM fabricated Fe₃Al alloy with inter-pass temperatures of 280, 320, 360, and 400 °C. Grain size increased when a reduced inter-pass

M. Karmuhilan and Somasundaram Kumanan, National Institute of Technology Tiruchirappalli, Tiruchirappalli, India. Contact e-mail: kumanan@nitt.edu.

temperature was employed, while yield strength increased when the inter-pass temperature increased. Ma et al. (Ref 24) investigated the effects of inter-pass temperatures (100, 200, 300, 400, and 500 °C) on in situ alloying of TiAl alloy using the WAAM method. They found that a slower cooling rate caused a drop in the α_2 phase fraction as the inter-pass temperature increased. The microhardness decreased as the inter-pass temperature increased. Cuiuri et al. examined how IPT affected additively manufactured TiAl alloy. Microhardness decreased when IPT rose from 100 to 400 °C (Ref 24). Francisco et al. created an ANN-based predictive model for the inter-pass temperature utilizing the FEM data from an investigation on the effects of idle time (30-240 s) on the inter-pass temperature (IT) of 20-layer single-bead walls manufactured using WAAM. The FEM simulations were performed using a heat source and a 20-layer single-bead wall model that had been empirically calibrated and confirmed (Ref 25). A unique method determines the idle times required to keep the molten pool size and inter-pass temperature constant during WAAM operations. The key idea is to compute the idle times necessary to obtain the predetermined inter-pass temperature while keeping track of how quickly each layer cools after being deposited using an FE simulation of the WAAM procedure (Ref 26). It is crucial to allow pauses between the deposition of subsequent layers so that the workpiece can cool down due to the significant heat transfer during this process. It also keeps the workpiece from collapsing and guarantees a proper inter-pass temperature. The investigation on the effect of inter-pass layer temperature on microstructural and mechanical properties of WAAM-printed Inconel 625 parts needs attention, and this paper discusses experimentation and analysis of the impact of change in inter-pass layer idle time on microstructural and mechanical properties of WAAM-printed Inconel 625 parts.

2. Experimental Details

2.1 Materials and Methods

The WAAM system used in the investigation includes a power supply and a GMAW welding torch connected with a 3-axis computer-controlled motion system, as shown in Fig. 1. The computer-controlled motion system controls the predefined path of deposition. The movement of the torch was controlled

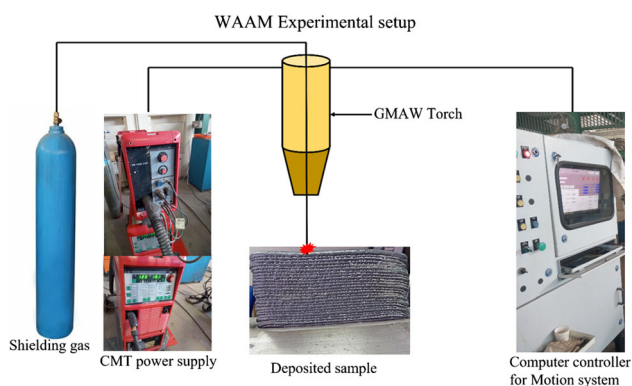


Fig. 1 Schematic diagram of the experimental setup of the WAAM system

by numerical programming. A Transpuls synergic 5000 (CMT) system with a Fronius VR 7000 CMT wire feeder system was used as a power supply. Inconel 625, 1.2 mm in diameter, was used as a filler wire, and the base plate (stainless steel 304) was 200 mm × 100 mm × 10 mm in dimension. The chemical composition of Inconel 625 wire and base plate is given in Tables 1 and 2, respectively. Before the trial, a steel wire brush cleaned the substrate to remove oxide buildup. The trial-and-error tests found the correct parameters for the defect-free deposition of beads. The following parameters are used during deposition: 15 mm standoff distance, 250 mm/min torch travel speed, 118 A current, 18.2 V voltage, and 4.2 m/min feed rate. The shielding gas used in GMAW was argon with a 16 lit/min flow rate. Inter-pass layer temperatures were 100, 200, and 300 °C for manufacturing three Inconel 625 walls. The industrial Infrared thermometer was used to measure the temperature of each layer to implement the inter-pass temperature strategy. Initially, the baseplate was heated to respective temperature, the first layer was deposited, and then the layer was allowed to cool at respective inter-pass temperatures after deposit. The fabricated additive structures are shown in Fig. 2. The dimensions of the fabricated additive structures are shown in Table 3.

2.2 Microstructural Characterization

Microstructural and mechanical analysis specimens were prepared using a wire-cut electrical discharge machine. The samples obtained from three Inconel walls were analyzed using optical micrographs, FESEM with EDS XRD, and EBSD analysis. The samples were extracted from the middle portion of the additive structures for microstructural examination. The sample surfaces were polished to a submicron level using several polishing grade sheets. The aqua regia mixture (1 part of nitric acid, three parts of hydrochloric acid, and two parts of glycerine) was used to etch the samples for thirty seconds. An optical microscope was used to take micrographs of all samples (Make: Olympus, Model: BX-41 M-LED). The elemental composition and surface morphology were investigated using an energy-dispersive x-ray spectroscope (EDS) and a field emission scanning electron microscope (FESEM) on a Carl Zeiss Gemini SEM S300H. The samples were prepared and polished electrolytically for Electron backscattered diffraction (EBSD) analysis. Fei Quanta-3D FEG equipment performed the EBSD analysis. Rigaku (miniflex600) was used for x-ray diffraction (XRD) analysis. XRD measurements were performed using Cu-K α radiation at 40 kV and 15 mA with a scan speed of 3.0 deg/min and step width of 0.02 deg.

2.3 Mechanical Characterization

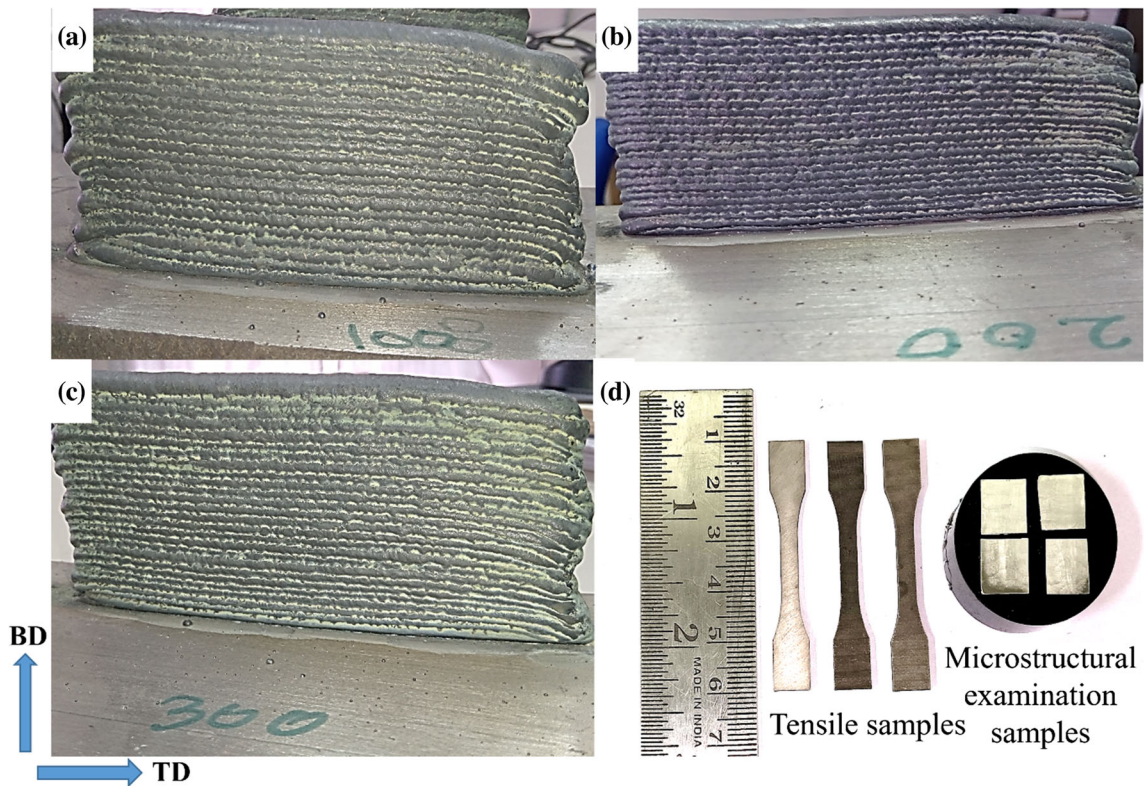
Mechanical tests, such as tensile and microhardness tests, were conducted to investigate the mechanical characteristics of Inconel 625 samples. The specimens were extracted from the additive structures longitudinally or parallel to the deposition layer. The specimens were prepared with ASTM E8 standards. Tensile tests with a 1 mm/min load rate were carried out on the Tinius Olsen H50KL universal testing machine. Three samples were tested for each 100, 200, and 300 °C IPTs to calculate the average values of tensile properties. Microhardness testing was done in Wilson Hardness VICKERS 402 MVD (1 kg load with a dwell of 10 s).

Table 1 Chemical composition of Inconel 625

Material	Cr	Fe	Mo	Nb	C	Mn	Si	Co	Al	Ti	Ni
Inconel 625	21	5.0	8.50	3.75	0.10	0.50	0.50	1.0	0.4	0.4	Bal.

Table 2 Chemical composition of stainless steel 304

Material	Cr	Ni	C	Mn	Si	P	S	N	Fe
Stainless steel 304	18.5	9.5	0.07	2.0	1.0	0.05	0.04	0.11	Bal.

**Fig. 2** (a) Sample deposited with 100 °C, (b) sample deposited with 200 °C, (c) sample deposited with 300 °C and (d) model samples for microstructure and tensile properties**Table 3 Dimensions of additively fabricated Inconel 625 walls using the WAAM process**

Inconel 625 wall/dimensions	Length, mm	Width, mm	Height, mm	No. of layers	Layer thickness, mm
IPT 100 °C	120 ± 2	9.8 ± 0.5	60 ± 1	22	2.7 ± 0.2
IPT 200 °C	120 ± 2	10.2 ± 0.5	60 ± 1	25	2.4 ± 0.2
IPT 300 °C	120 ± 2	10.5 ± 0.5	60 ± 1	26	2.3 ± 0.2

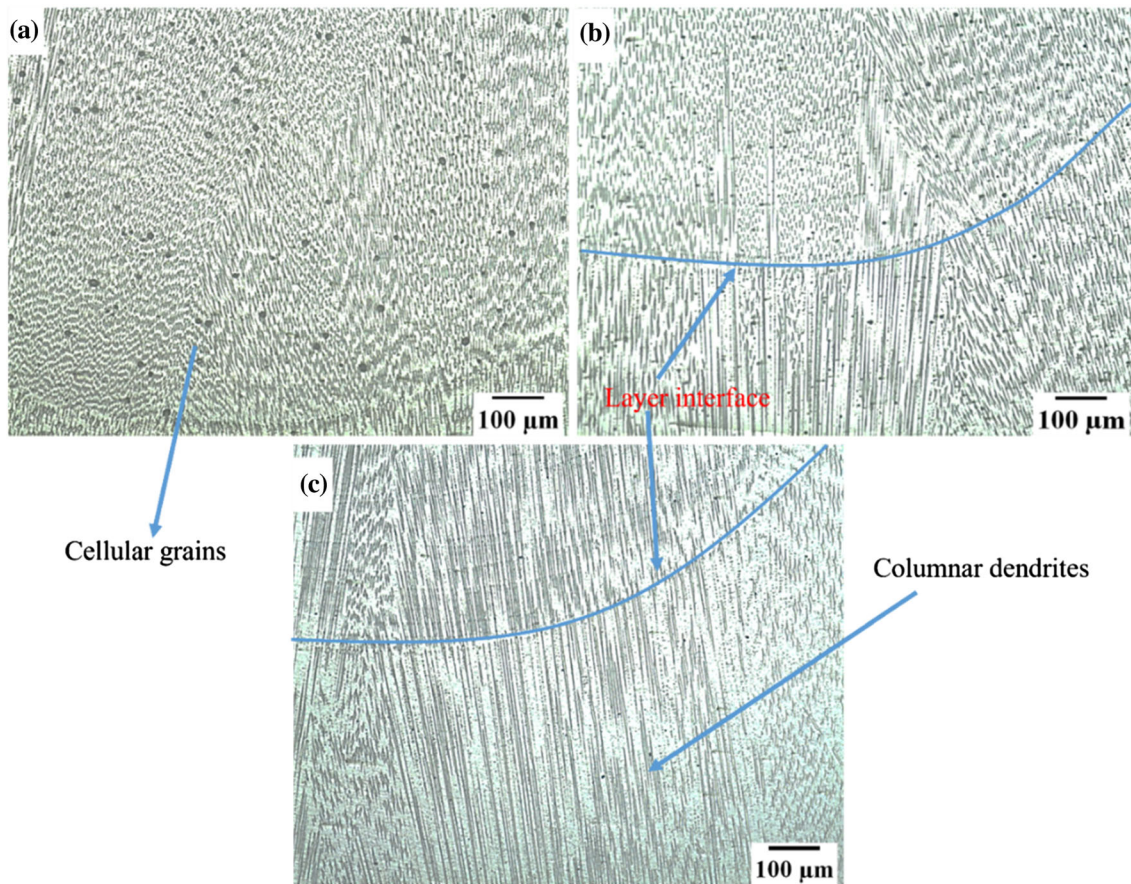


Fig. 3 Optical micrograph of WAAM-processed Inconel 625 for different inter-pass temperatures: (a) 100 °C, (b) 200 °C, and (c) 300 °C

3. Results and Discussion

3.1 Microstructural Examination

3.1.1 Microstructure and Elemental Composition Analysis. Figure 3 shows the observed optical micrographs showing differences in the Inconel 625 microstructure for three inter-pass temperatures. The grain morphology relies on the solidification rate, undercooling, temperature gradient (G), and melt composition. These factors determine the type of microstructure. Most metal alloys form cellular or columnar dendritic patterns when it solidify (Ref 27). The direction of the heat flux causes the grains to grow vertically. Therefore, as the melt pool solidified, grain growth was practically perpendicular to the baseplate (Ref 28). The sample deposited with 100 °C as inter-pass temperature consists of cellular grains, as shown in Fig. 3(a). The sample, which had an inter-pass temperature of 200 °C, has a combo of cellular grains and columnar dendrites, as shown in Fig. 3(b). In the IPT 300 °C sample, columnar dendrites were found in the majority, as in Fig. 3(c).

The schematic representation of the heat accumulation behavior of deposited additive structures is shown in Fig. 4. The intensity of heat accumulation varied in different inter-pass layer temperatures. In Fig. 4(c), the dark red represents the higher heat accumulated in the IPT 300 °C sample. This phenomenon occurs due to the continuous deposition of beads at higher inter-pass layer temperatures. The cooling occurs primarily via previously deposited layers and substrates in the CMT-WAAM process. A finer microstructure is produced at a

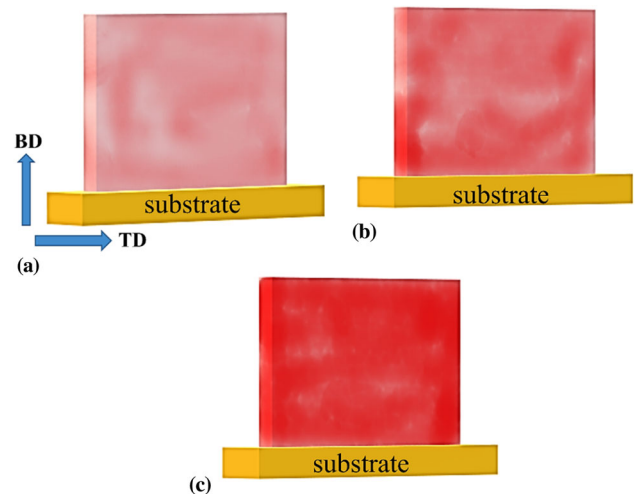


Fig. 4 Schematic representation of Heat accumulation behavior of WAAM-printed samples with different IPTs (BD-Building Direction, TD-Travel Direction): (a) 100 °C, (b) 200 °C, and (c) 300 °C

higher cooling rate (Ref 29). In IPT 300 °C, the previously deposited layer remains 300 °C, and the bead is deposited one over another in the same manner. So, the temperature of the previously deposited layer and substrate remains higher, reducing the heat dissipation. The thermal gradient and the cooling rate were reduced in the IPT 300 °C sample. At the same time, the other samples have reduced heat accumulation

due to considerable heat dissipation, as shown in Fig. 4(a) and (c).

The proportional relationship between cooling rate and inter-pass layer temperature is shown in Eq 1, where H.I is the heat input (kJ mm^{-1}), CR is the cooling rate ($^{\circ}\text{C s}^{-1}$), and T_0 is the inter-pass layer temperature. Additional factors that affect the cooling rate include thermal conductivity, specific heat, density of the material being welded, part dimensions and thickness, welding position, and ambient temperature (Ref 30).

$$\text{CR} \propto \frac{1}{T_0 \cdot \text{H.I}} \quad (\text{Eq 1})$$

According to Eq 2, “heat input” is the energy used for each welding length during arc welding. Here, η is the arc efficiency, a non-dimensional coefficient that is regarded as 0.99 for welding, and H.I is the heat input (KJ mm^{-1}), I is the Welding Current (A), V is the Voltage (V), and S is the welding speed (mm s^{-1}) (Ref 31).

$$\text{H.I} = \frac{V \cdot I \cdot \eta}{S} \quad (\text{Eq 2})$$

Equation 1 gives the cooling rate of each deposited sample with different inter-pass layer temperatures. Here, the net heat input is constant as the voltage (V), current (A), and welding speed (S) are the fixed parameters. From the above proportional equation, as the T_0 increases, the cooling rate decreases. Due to the increased inter-pass layer temperature, the cooling rate reduces and affects the microstructure and mechanical properties.

The following explanation relates to the observed microstructures: A change in heat accumulation caused by a difference in the inter-pass layer temperatures causes the most significant temperature gradient at the melt pool boundary to rotate over time. In order to follow the highest temperature gradient, the preferred direction for grain growth is the opposite of the direction for unidirectional heat flux. The grains tilt in the direction of the heat source because they always grow in the direction of the fastest heat dissipation. The grain growth direction is precisely perpendicular to the substrate if the substrate and previously deposited layer are used to cool the molten pool completely. Although the baseplate and previously deposited layer are the primary means of cooling the molten pool, the cooling occurs partly through the adjacent solidified deposited layer at the rear side of the weld pool. So, the grain growth direction is somehow tilted from the previously deposited layer.

$$G = \frac{C \cdot R}{R} \quad (\text{Eq 3})$$

The above Eq 3 defines the thermal gradient (G), and it depends on the cooling rate and growth rate (Ref 32). During solidification, grain structure depends on the temperature gradient (G) and the growth rate (R), as shown in Fig. 5. The grain structure can be defined using the G/R ratio (Ref 33, 34). Inter-pass layer temperature plays a vital role in grain morphology in the WAAM process. Since the welding speed of the torch in the Travel direction is stable, the growth rate (R) is constant. However, the temperature gradient (G) reduced when the inter-pass layer temperatures increased from 100 to 300 $^{\circ}\text{C}$ due to the difference in cooling rate. The calculated values of cooling rate (CR), growth rate (R), and Temperature

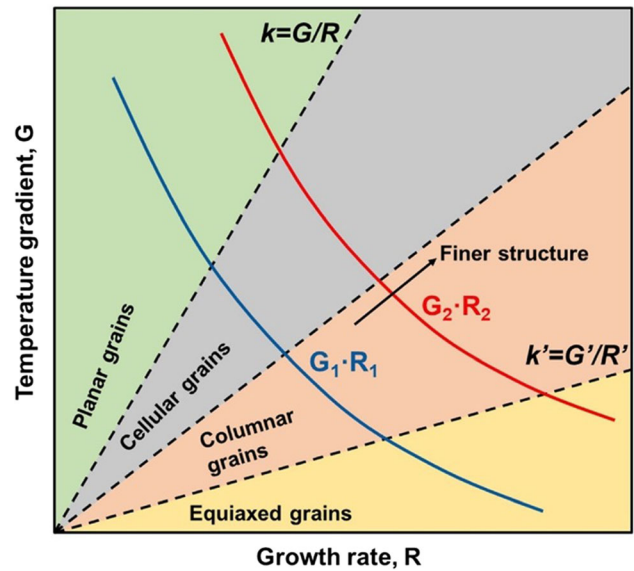


Fig. 5 Schematic explanation of temperature gradient(G) and growth rate(R) for solidification morphology (Ref 33). Reprinted from *Journal of Manufacturing Processes*, Vol 50, Hang Zhao, Guotao Zhang, Qingxin Zhang, Chaoqun Zhang, Yongbing Li, Joining mechanism and mechanical properties of metallic bump assisted weld-bonded (MBaWB) joints of AA6061-T6 and bare DP590, Pages 204-215, Copyright 2020, with permission from Elsevier

gradient (G) are shown in Table 4. Here, the value of the G/R ratio decreases for two reasons: (a). the R is constant, and (b). IPT changes from 100 to 300 $^{\circ}\text{C}$. When the IPT changed from 100 to 300 $^{\circ}\text{C}$, the cooling rate was reduced as the cooling rate is the function of inter-pass layer temperature as given in Eq 1. The temperature gradient is directly proportional to the cooling rate; it reduces when the cooling rate is reduced, as given in Eq 3. The solidification trend shifts from planar to cellular, cellular to columnar dendrite, and columnar dendrite to equiaxed dendrite, respectively, as the G/R ratio is reduced (Ref 35). From the above, it is defined that the inter-pass layer temperature is inversely proportional to a temperature gradient and affects the G/R ratio. The G/R ratio reduced when the inter-pass layer temperature increased from 100 to 300 $^{\circ}\text{C}$. The grain structure transformed from cellular to columnar dendrites as the IPT changed from 100 to 300 $^{\circ}\text{C}$. A high G/R ratio promotes the cellular grains in the IPT 100 $^{\circ}\text{C}$ sample. When the G/R reduces, the IPT 200 and IPT 300 $^{\circ}\text{C}$ samples transform into a mixture of cellular and columnar and Columnar dendrites, respectively.

The surface morphology and EDS spectrum of the three samples are shown in Fig. 6. The EDS findings show that the amount of Nb is lower at IPT 300 $^{\circ}\text{C}$ (Fig. 6c) compared to IPT 100 and 200 $^{\circ}\text{C}$ samples (Fig. 6a and b), with a difference of about 2-3%, followed by Cr and Mo elements. Co, Si, and Fe exhibit slight variation according to EDS analysis. The enrichment of vital alloying elements appears to have decreased in the IPT 300 $^{\circ}\text{C}$ sample compared to the IPT 100 and 200 $^{\circ}\text{C}$ samples. According to EDS results, the sample deposited with IPT 300 $^{\circ}\text{C}$ had a smaller content of Cr, Nb, and Mo than that deposited with other samples.

Table 4 Calculated values of cooling rate (CR), growth rate (*R*) and temperature gradient (*G*) for different IPTs

S. no	Heat input (H. I), KJ/mm	Inter-pass layer temperature, T_0 , °C	Cooling rate (CR), °C/s	<i>R</i> , mm/s	<i>G</i> , °C/mm	<i>G/R</i>
1	0.515	100	33.460	4.166	8.030	1.927
2	0.515	200	21.510	4.166	5.162	1.239
3	0.515	300	11.950	4.166	2.868	0.688

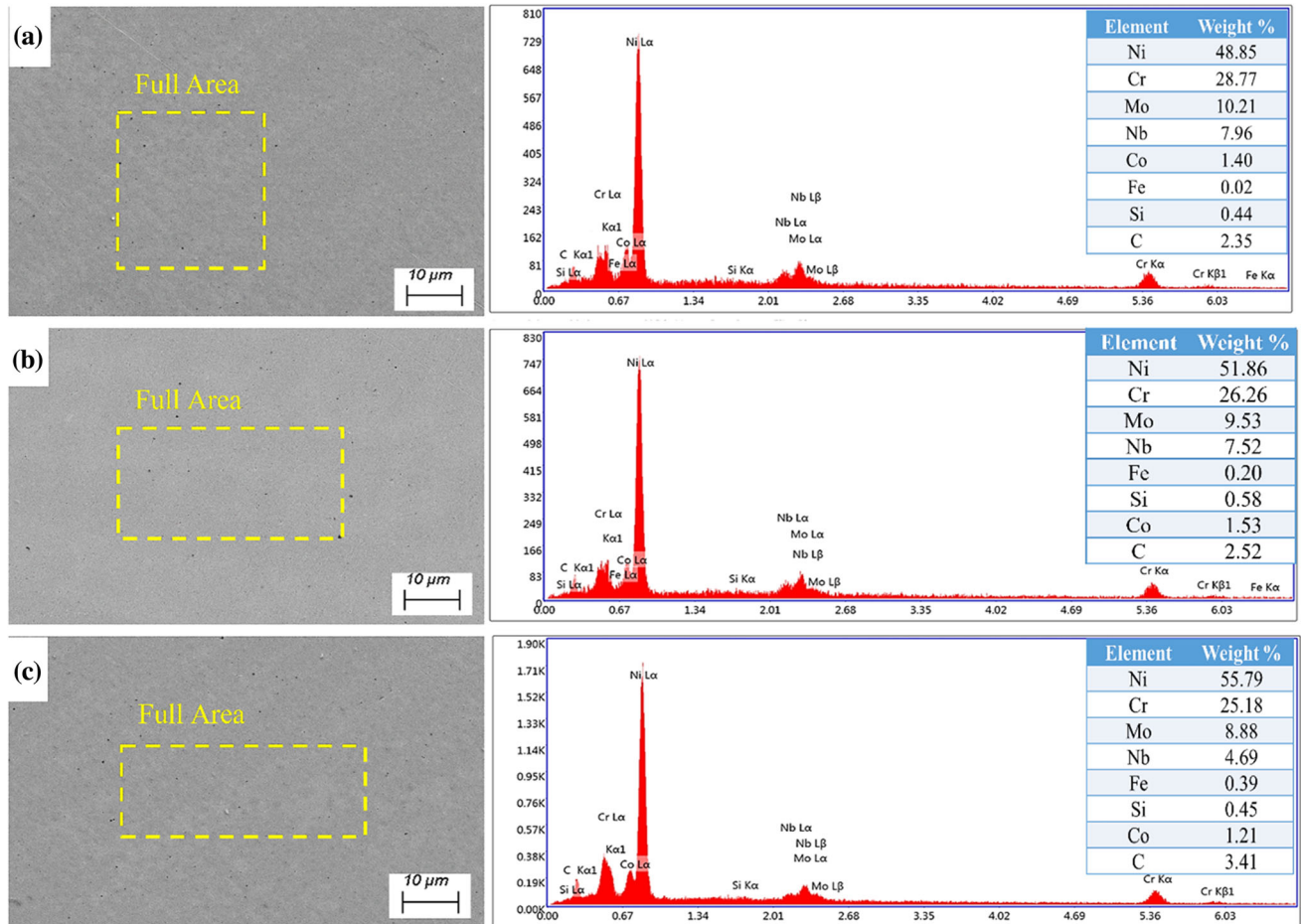


Fig. 6 EDS analysis of WAAM-printed Inconel 625 samples with IPT: (a) 100 °C, (b) 200 °C, and (c) 300 °C

3.1.2 Grain Size and Grain Distribution Analysis Using EBSD. The color map with inverse pole figure and grain size distribution chart of three different IPT samples are shown in Fig. 7. The map depicts the grain boundary, size, and growth direction of the three samples. The grain growth appeared along the building direction and followed the higher temperature gradient (Ref 36). The color red represents $\langle 001 \rangle$ and $\langle 101 \rangle$ for green and $\langle 111 \rangle$ for blue, as shown in the standard stereographic triangle Fig. 7(a). The grains are randomly orientated for all the samples. The grain size of the 100 °C sample is considerably smaller than the other two samples, as shown in Fig. 7(b), (d), (f). The average grain size of the 100 °C sample is obtained as 30.83 μm . At the same time, the average grain size of IPT 200 and IPT 300 °C samples are 54.13 and 70.77 μm , respectively. The variation in grain size is achieved due to different cooling rates, and heat

accumulation occurs in different IPTs. The welding idle time was reduced because of the increased IPT. Higher IPTs lowered the thermal gradient and lengthened the cooling process (Ref 37). The inter-pass temperature increase led to lower weld metal strength and hardness and larger grains (Ref 38). The cooling rate of IPT 100 °C is noticeably faster than other IPT samples, which causes a smaller grain size. The slow cooling occurred at IPT 300 °C due to considerable heat accumulation. Hence, the grain size in IPT 300 °C is noticeably more prominent than the other.

The grain boundary distribution diagram and its histogram of three IPT samples are displayed in Fig. 8. The high-angle grain boundary (HAGB) is greater than 15°, and the low-angle grain boundary (LAGB) is less than 15°. In LAGB, 1-5° and 5-15° are shown in red and green, respectively. Blue is used to signify the HAGB (>15°). As a result of dislocation rearrangement, LAGB (1-5°) is formed as a sub-grain boundary. The proportion of

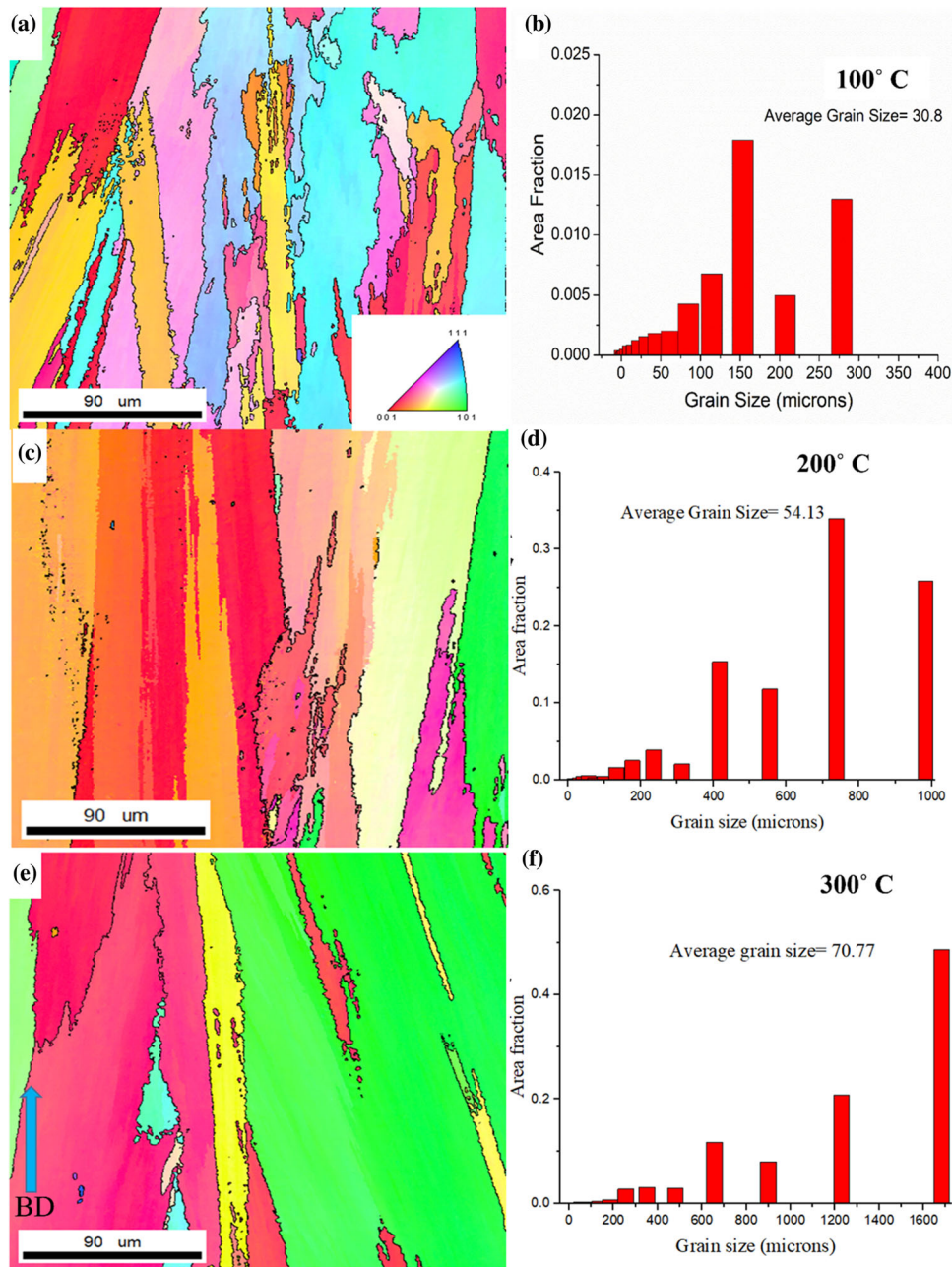


Fig. 7 EBSD color map with inverse pole figure (IPF) (a, c, e) and grain size distribution chart (b, d, f) (BD-Building Direction): (i) a, b – 100 °C, (ii) c, d – 200 °C, and (iii) e, f-300 °C

HAGB in the IPT 100 °C sample is higher than in the other two samples. The IPT 200 and IPT 300 °C samples have a mixed proportion of LAGB and HAGB. IPT 100 °C sample has lower volumes of sub-grain boundaries, suggesting less LAGB production during this temperature. HAGB can act as obstacles to dislocation motion, enhancing the mechanical strength of a material. The existence of several high-angle grain boundaries can enhance hardness, tensile strength, and deformation resistance. HAGBs may occasionally provide greater ductility in materials. They can function as sites for plastic deformation, allowing localized deformation and strain accommodation without producing catastrophic failure (Ref 39).

3.1.3 X-ray Diffraction (XRD) Analysis. Inconel 625 has a face-centered cubic (FCC) crystal structure, and its XRD pattern will often display diffraction peaks that correspond to the lattice planes of an FCC structure. The most prominent diffraction peak is often the (111) plane, followed by peaks like (200), (220), and others (Ref 40). The positions and intensities of these peaks can vary depending on sample preparation, crystallographic orientation, and any potential secondary phases. However, according to the ICDD database, the most significant positions for pure Ni were 44.4, 51.9, and 76.4° (Ref 41, 42). The XRD patterns of the three samples under investigation are shown in Fig. 9. The primary crystal orientation peaks, achieved at 2θ values for three IPTs, are

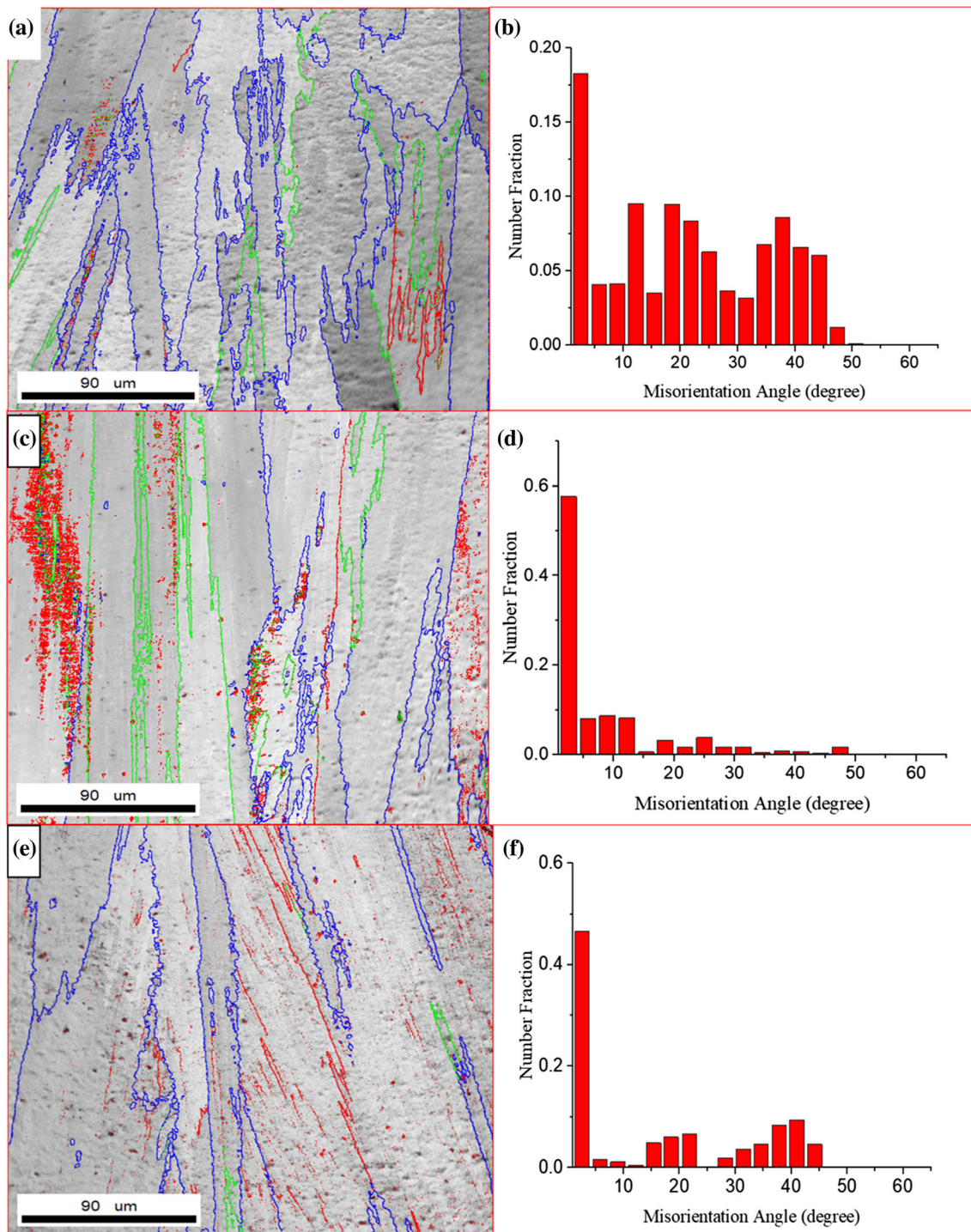


Fig. 8 Grain boundary distribution diagram (a, c, e) and histogram (b, d, f): (i) a, b – 100 °C, (ii) c, d – 200 °C, and (iii) e, f –300 °C

(111), (200), and (220). The peak position at 2θ values of IPT 100 °C samples are 42.554 (111), 49.626 (200), and 73.694° (220). It was reported in the previous study that the peaks at 2θ values obtained for the IPT 200 °C sample are as follows: 43.018 (111), 50.33 (200), 73.92° (220). However, the peak positions of the IPT 300 °C sample are obtained as 43.980 (111), 51.160 (200), and 75.208° (220). The XRD could only

detect the Ni-base austenitic phase (γ Phase) for all samples. Other intermetallic phases of the Ni matrix are not detected due to the low volume fraction of such phases. Peak locations for the IPT 100 °C sample differ slightly from those for the IPT 200 and 300 °C samples. For the IPT 100 and 200 °C samples, the γ -Ni FCC (111) is set to the favored crystal orientation due to the high peak intensity at 2θ value of 42.554 and 43.018°, as

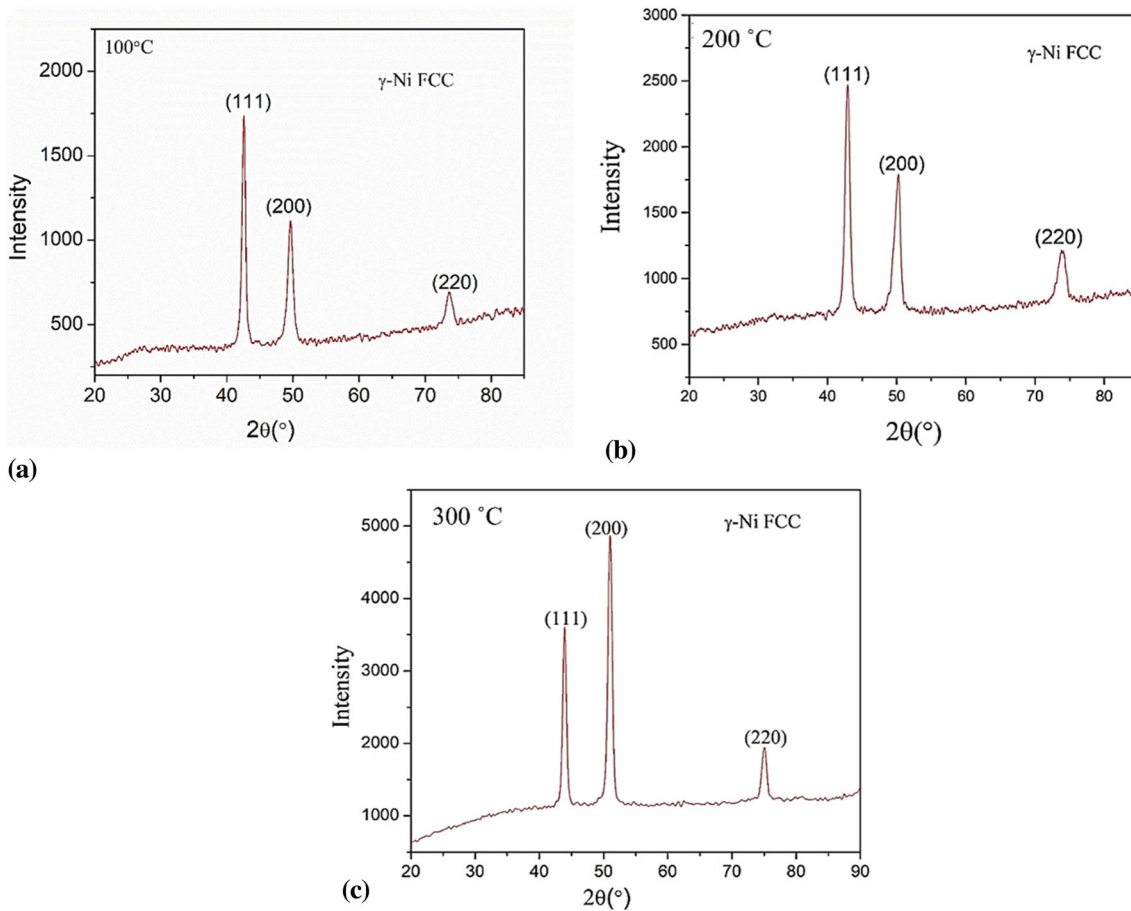


Fig. 9 XRD patterns for WAAM-processed samples with different IPTs

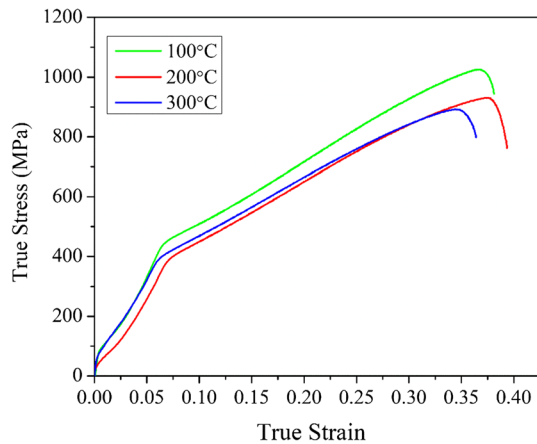


Fig. 10 Tensile Curves of Inconel 625 parts for three IPT samples

shown in Fig. 9(a) and (b). For the IPT 300 °C sample, γ -Ni FCC (200) is set to the preferred crystal orientation due to the high peak intensity at 51.160°, as shown in Fig. 9(c).

3.2 Mechanical Properties

The tensile curves achieved in various IPT samples are shown in Fig. 10. The sample, made at IPT 100 °C, possesses superior mechanical properties over other samples. The obtained tensile properties are shown in Table 5. The ultimate tensile strength (UTS) 664 ± 5 to 713 ± 9 MPa and yield strength (YS) 382 ± 2 to 422 ± 5 MPa increased with a decrease in IPTs, and elongation changed from 43.9 to 48.1%. According to the Hall–Petch theory, the mechanical properties are inversely correlated with grain size (Ref 43, 44). The grain size can be seen in the EBSD color map for all IPTs. This variation in tensile properties is achieved due to the difference

Table 5 Tensile properties for various inter-pass layer temperatures

Inter-pass layer temperature, °C	Yield strength, MPa	Ultimate tensile strength, MPa	Elongation %
100	422 ± 5	713 ± 9	43.9
200	402 ± 4	678 ± 7	46.3
300	382 ± 2	664 ± 5	48.1

in the microstructure, as the smaller grains can somewhat enhance the mechanical properties. Grain boundaries can influence the mechanical behavior of materials. HAGB improves the mechanical behavior because it is a barrier to dislocation motion. A higher HAGB density may be advantageous to obtain high strength in structural applications. The proportion of HAGB in the IPT 100 °C sample is higher than in the other two samples. The IPT 200 °C and IPT 300 °C samples have a mixed ratio of LAGB and HAGB. The higher proportion of HAGB promotes the strength in the IPT 100 °C sample, whereas the mixed ratio of HAGB and LAGB shows moderate strength. In this instance, the presence of HAGB in IPT 100 °C improved the mechanical properties of WAAM-processed samples.

The microhardness values are tested in all three IPT samples for five repetitions. The test samples are taken from the middle of the additive structure. The test values are taken in an interval of 1 mm distance, and the results are shown in Fig. 11. The average microhardness of the IPT 100, IPT 200, and IPT 300 °C samples are 260.2 ± 2 , 249.78 ± 3 , and 233.7 ± 3 HV, respectively. The hardness value increased when the IPT decreased. The microstructure evaluation section gives the average grain size of all samples. The hardness value is inversely proportional to the grain size. The grain size of the IPT 300 °C sample is more prominent than the IPT 200 °C sample, so the microhardness value is less than the other samples.

4. Conclusion

Three Inconel 625 parts were fabricated using the wire and arc AM technique with different inter-pass layer temperatures. The microstructure and mechanical characterization were analyzed.

- The results showed that the grain morphology varied as cellular, the mixture of a cellular and columnar dendrite, and the majority of columnar dendrites for 100, 200, and 300 °C, respectively.
- A high G/R ratio promotes the cellular grains in the IPT 100 °C sample. The IPT 200 °C and IPT 300 °C samples

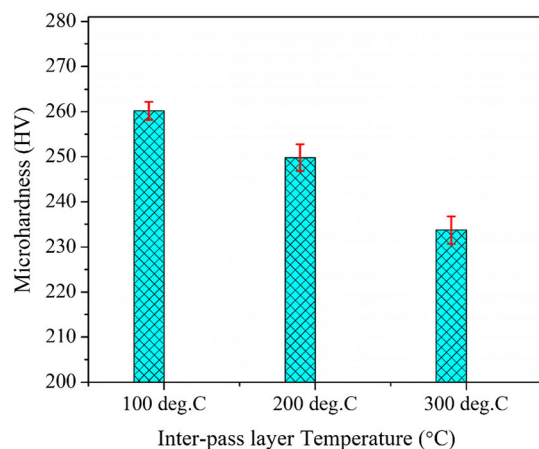


Fig. 11 Microhardness values of WAAM-processed samples in different IPTs

change into mixtures of cellular, columnar, and columnar dendrites, respectively, when the G/R lowers.

- The SEM with EDS examined the elemental composition of both samples. The sample deposited with IPT 300 °C has a lower content of Cr, Nb, and Mo than the sample deposited with other samples.
- The EBSD color map shows the grain boundaries and size for all samples. The grain size increased from 30.83 to 70.77 μm as the IPT changed from 100 to 300 °C. The slow cooling due to considerable heat accumulation increased the grain size in IPT 300 °C. The proportion of HAGB is more significant for the IPT 100 °C sample.
- The prominent crystal orientation peaks (111), (200), and (220) discovered at 2θ values for both samples were identified by the XRD analysis. Apart from the γ -Ni FCC phase, the remaining phases are not observed.
- When the IPT was changed from 300 to 100 °C, the ultimate tensile strength improved from 664 ± 5 to 713 ± 9 MPa and the yield strength from 382 ± 2 to 422 ± 5 MPa. The obtained microhardness value of the IPT 100 °C sample is higher than that of another sample due to variation in grain size.

Conflict of interest

The authors declare that they have no known competing financial interests or personal relationships that could have appeared to influence the work reported in this paper.

References

1. M. Liu, Q. Wang, Y. Cai, D. Lu, Y. Pei, H. Zhang, Y. Liu, and Q. Wang, Dependence on Manufacturing Directions of Tensile Behavior and Microstructure Evolution of Selective Laser Melting Manufactured Inconel 625, *J. Mater. Eng. Perform.*, 2022 <https://doi.org/10.1007/s11665-022-07622-6>
2. F. Wang, H. Liu, J. Li, H. Wan, L. Yu, and B. Liu, Microstructure Evolution and Mechanical Properties of Inconel 625 Foils, *J. Mater. Eng. Perform.*, 2023 <https://doi.org/10.1007/s11665-023-08114-x>
3. X. Yu, J. Xue, Q. Shen, Z. Zheng, N. Ou, and W. Wu, Dual-Wire Plasma Arc Additively Manufactured SS 316L-Inconel 625 Functionally Graded Material: Microstructure Evolution and Mechanical Properties, *J. Mater. Eng. Perform.*, 2023, **32**(3), p 1412–1422. <http://doi.org/10.1007/s11665-022-07158-9>
4. T. Borowski, A. Brojanowska, M. Kost, H. Garbacz, and T. Wierchoń, Modifying the Properties of the Inconel 625 Nickel Alloy by Glow Discharge Assisted Nitriding, *Vacuum*, 2009, **83**(12), p 1489–1493.
5. E.O. Olakanmi, S.T. Nyadongo, K. Malikonwa, S.A. Lawal, A. Botes, and S.L. Pityana, Multi-Variable Optimisation of the Quality Characteristics of Fiber-Laser Cladded Inconel-625 Composite Coatings, *Surf. Coat. Technol.*, 2019, **357**, p 289–303. <https://doi.org/10.1016/j.surfcoat.2018.09.063>
6. F.A. Khalid, N. Hussain, and A.H. Qureshi, Microstructural Study on Oxidation of Aluminized Coating on Inconel 625, *J. Mater. Eng. Perform.*, 2002, **11**(2), p 211–214.
7. L. Mataveli Suave, J. Cormier, D. Bertheau, P. Villechaise, A. Soula, Z. Hervier, and F. Hamon, High Temperature Low Cycle Fatigue Properties of Alloy 625, *Mater. Sci. Eng. A*, 2016, **650**, p 161–170. <https://doi.org/10.1016/j.msea.2015.10.023>
8. M. Karmuhilan and S. Kumanan, A Review on Additive Manufacturing Processes of Inconel 625, *J. Mater. Eng. Perform.*, 2021 <https://doi.org/10.1007/s11665-021-06427-3>
9. S. Fan, X. Guo, Z. Li, J. Ma, F. Li, and Q. Jiang, A Review of High-Strength Aluminum-Copper Alloys Fabricated by Wire Arc Additive Manufacturing, *J. Mater. Eng. Perform.*, 2023 <https://doi.org/10.1007/s11665-023-08233-5>

10. B.K. Chigilipalli, Investigation of Microstructural Properties and Mechanical Behavior of Wire Arc Additively Manufactured Incoloy 825, *J. Mater. Eng. Perform.*, 2023 <https://doi.org/10.1007/s11665-023-08195-8>
11. B. Tomar, S. Shiva, and T. Nath, A Review on Wire Arc Additive Manufacturing: Processing Parameters, Defects, Quality Improvement and Recent Advances, *Mater. Today Commun.*, 2022, **31**, p 103739. <https://doi.org/10.1016/j.mtcomm.2022.103739>
12. A. Mishra, A. Raj, M. Mukherjee, and R.K. Singh, Bimetallic Structure of Ti6Al4V/IN718 with CuSi Interlayer for Wire-Arc Directed Energy Deposition Process, *Met. Mater. Int.*, 2023 <https://doi.org/10.1007/s12540-022-01381-8>
13. A.R. Kannan, S.M. Kumar, R. Pramod, N.S. Shanmugam, M. Vishnukumar, and S.G. Channabasavanna, Microstructure and Corrosion Resistance of Ni-Cu Alloy Fabricated through Wire Arc Additive Manufacturing, *Mater. Lett.*, 2022, **308**, p 131262. <https://doi.org/10.1016/j.matlet.2021.131262>
14. S. Selvi, A. Vishvakshan, and E. Rajasekar, Cold Metal Transfer (CMT) Technology—An Overview, *Def. Technol.*, 2018, **14**(1), p 28–44. <https://doi.org/10.1016/j.dt.2017.08.002>
15. X. Yin, G. He, W. Meng, Z. Xu, L. Hu, and Q. Ma, Comparison Study of Low-Heat-Input Wire Arc-Fabricated Nickel-Based Alloy by Cold Metal Transfer and Plasma Arc, *J. Mater. Eng. Perform.*, 2020, **29**(7), p 4222–4232. <https://doi.org/10.1007/s11665-020-04942-3>
16. B. Wu, D. Ding, Z. Pan, D. Cuiuri, H. Li, J. Han, and Z. Fei, Effects of Heat Accumulation on the Arc Characteristics and Metal Transfer Behavior in Wire Arc Additive Manufacturing of Ti6Al4V, *J. Mater. Process. Technol.*, 2017, **250**, p 304–312. <https://doi.org/10.1016/j.jmatprotec.2017.07.037>
17. B. Wu, Z. Pan, D. Ding, D. Cuiuri, and H. Li, Effects of Heat Accumulation on Microstructure and Mechanical Properties of Ti6Al4V Alloy Deposited by Wire Arc Additive Manufacturing, *Addit. Manuf.*, 2018, **23**, p 151–160. <https://doi.org/10.1016/j.addma.2018.08.004>
18. F. Montevecchi, G. Venturini, N. Grossi, A. Scippa, and G. Campatelli, Heat Accumulation Prevention in Wire-Arc-Additive-Manufacturing Using Air Jet Impingement, *Manuf. Lett.*, 2018, **17**, p 14–18. <https://doi.org/10.1016/j.mfglet.2018.06.004>
19. B. Wu, Z. Pan, D. Ding, D. Cuiuri, H. Li, and Z. Fei, The Effects of Forced Interpass Cooling on the Material Properties of Wire Arc Additively Manufactured Ti6Al4V Alloy, *J. Mater. Process. Technol.*, 2018, **258**, p 97–105. <https://doi.org/10.1016/j.jmatprotec.2018.03.024>
20. F. Montevecchi, G. Venturini, N. Grossi, A. Scippa, and G. Campatelli, Idle Time Selection for Wire-Arc Additive Manufacturing: A Finite Element-Based Technique, *Addit. Manuf.*, 2018, **21**, p 479–486. <https://doi.org/10.1016/j.addma.2018.01.007>
21. Y. Ma, D. Cuiuri, C. Shen, H. Li, and Z. Pan, Effect of Interpass Temperature on In-Situ Alloying and Additive Manufacturing of Titanium Aluminides Using Gas Tungsten Arc Welding, *Addit. Manuf.*, 2015, **8**, p 71–77. <https://doi.org/10.1016/j.addma.2015.08.001>
22. W. Yangfan, C. Xizhang, and S. Chuanchu, Microstructure and Mechanical Properties of Inconel 625 Fabricated by Wire-Arc Additive Manufacturing, *Surf. Coat. Technol.*, 2019, **374**(May), p 116–123. <https://doi.org/10.1016/j.surfcoat.2019.05.079>
23. C. Shen, Z. Pan, D. Cuiuri, D. Ding, and H. Li, Influences of Deposition Current and Interpass Temperature to the Fe3Al-Based Iron Aluminide Fabricated Using Wire-Arc Additive Manufacturing Process, *Int. J. Adv. Manuf. Technol.*, 2017, **88**(5), p 2009–2018. <https://doi.org/10.1007/s00170-016-8935-3>
24. Y. Ma, D. Cuiuri, C. Shen, H. Li, and Z. Pan, Effect of Interpass Temperature on In-Situ Alloying and Additive Manufacturing of Titanium Aluminides Using Gas Tungsten Arc Welding, *Addit. Manuf.*, 2015, **8**, p 71–77.
25. V. Hugo, P. Moraes, F. Werley, and C. Farias, Prediction of the Interpass Temperature of a Wire Arc Additive Manufactured Wall: FEM Simulations and Artificial Neural Network o Da Cruz Pay A, *Addit. Manuf.*, 2021, **48**, p 102387.
26. Y. Lei, J. Xiong, and R. Li, Effect of Inter Layer Idle Time on Thermal Behavior for Multi-Layer Single-Pass Thin-Walled Parts in GMAW-Based Additive Manufacturing, *Int. J. Adv. Manuf. Technol.*, 2018, **96**(1–4), p 1355–1365.
27. Y. Lee, M. Nordin, S.S. Babu, and D.F. Farson, Effect of Fluid Convection on Dendrite Arm Spacing in Laser Deposition, *Mater. Trans.*, 2014, **45**, p 1520–1529.
28. J. Nguejio, F. Szmytka, S. Hallais, A. Tanguy, S. Nardone, and M. Godino Martinez, Comparison of Microstructure Features and Mechanical Properties for Additive Manufactured and Wrought Nickel Alloys 625, *Mater. Sci. Eng. A*, 2019, **764**, p 138214. <https://doi.org/10.1016/j.msea.2019.138214>
29. Y. Chen, M. Xu, T. Zhang, J. Xie, K. Wei, S. Wang, L. Yin, and P. He, Grain Refinement and Mechanical Properties Improvement of Inconel 625 Alloy Fabricated by Ultrasonic-Assisted Wire and Arc Additive Manufacturing, *J. Alloys Compd.*, 2022, **910**, p 164957. <https://doi.org/10.1016/j.jallcom.2022.164957>
30. K. Sirin, S.Y. Sirin, and E. Kaluc, Influence of the Interpass Temperature on t 8/5 and the Mechanical Properties of Submerged Arc Welded Pipe, *J. Mater. Process. Technol.*, 2016, **238**, p 152–159. <https://doi.org/10.1016/j.jmatprotec.2016.07.008>
31. K. Poorhaydari, B.M. Patchett, and D.G. Ivey, Estimation of Cooling Rate in the Welding of Plates with Intermediate Thickness, *Weld. J.*, 2005, **84**, p 149–155.
32. A.P. Silva, A. Garcia, and J.E. Spinelli, Microstructure Morphologies during the Transient Solidification of Hypomonotectic and Monotectic Al-Pb Alloys Microstructure Morphologies during the Transient Solidification of Hypomonotectic and Monotectic Al-Pb Alloys, *J. Alloys Compd.*, 2011, **509**(41), p 10098–10104. <https://doi.org/10.1016/j.jallcom.2011.08.049>
33. H. Zhao, G. Zhang, Q. Zhang, C. Zhang, and Y. Li, Joining Mechanism and Mechanical Properties of Metallic Bump Assisted Weld-Bonded (MBaWB) Joints of AA6061-T6 and Bare DP590, *J. Manuf. Process.*, 2020, **50**, p 204–215. <https://doi.org/10.1016/j.jmapro.2019.12.018>
34. K. Liu, Z. Yan, F. Wang, K. Li, S. Lin, and S. Chen, Microstructure, Texture and Mechanical Properties of Inconel GH4169 Superalloy Fabricated by Wire Arc Additive Manufacturing with Arc Oscillation, *J. Alloys Compd.*, 2023, **952**, p 170070. <https://doi.org/10.1016/j.jallcom.2023.170070>
35. S.H. Baghjari and S.A.A. Akbarimousavi, Experimental Investigation on Dissimilar Pulsed Nd: YAG Laser Welding of AISI 420 Stainless Steel to Kovar Alloy, *J. Mater.*, 2014, **57**, p 128–134. <https://doi.org/10.1016/j.matdes.2013.12.050>
36. J.F. Wang, Q.J. Sun, H. Wang, J.P. Liu, and J.C. Feng, Effect of Location on Microstructure and Mechanical Properties of Additive Layer Manufactured Inconel 625 Using Gas Tungsten Arc Welding, *Mater. Sci. Eng. A*, 2016, **676**, p 395–405. <https://doi.org/10.1016/j.msea.2016.09.015>
37. P. Henrique, G. Dornelas, F. Werley, C. Farias, V. Hugo, and P. Moraes, Influence of the Interpass Temperature on the Microstructure and Mechanical Properties of the Weld Metal (AWS A5. 18 ER70S-6) of a Narrow Gap Welded API 5L X70 Pipe Joint, *Int. J. Press. Vessels Pip.*, 2022, **199**, p 104690.
38. X.L. Wang, Y.T. Tsai, J.R. Yang, Z.Q. Wang, X.C. Li, and C.J. Shang, Effect of Interpass Temperature on the Microstructure and Mechanical Properties of Multi-pass Weld Metal in a 550-MPa-Grade Offshore Engineering Steel, *Welding in the World*, 2017, **61**, p 1155–1168.
39. C. Hu, C. He, X. Gan, X. Wan, F. Hu, W. Zhou, H. Wang, and K. Wu, Probing the Impact of Grain Interior and Grain Boundaries on the Mechanical Behavior of a High-Mn Austenitic Steel, *J. Mater. Res. Technol.*, 2022, **21**, p 5098–5110. <https://doi.org/10.1016/j.jmrt.2022.11.085>
40. M. Karmuhilan and S. Kumanan, Location-Dependent Microstructure Analysis and Mechanical Behavior of Inconel 625 Using Cold Metal Transfer(CMT) Based Wire and Arc Additive Manufacturing, *Vacuum*, 2023, **207**, p 111682.
41. T.E. Abioye, D.G. McCartney, and A.T. Clare, Laser Cladding of Inconel 625 Wire for Corrosion Protection, *J. Mater. Process. Technol.*, 2015, **217**, p 232–240. <https://doi.org/10.1016/j.jmatprotec.2014.10.024>
42. K. Feng, Y. Chen, P. Deng, Y. Li, H. Zhao, F. Lu, R. Li, J. Huang, and Z. Li, Improved High-Temperature Hardness and Wear Resistance of Inconel 625 Coatings Fabricated by Laser Cladding, *J. Mater. Process. Technol.*, 2017, **243**, p 82–91. <https://doi.org/10.1016/j.jmatprotec.2016.12.001>
43. Y. Chen, M. Xu, T. Zhang, J. Xie, K. Wei, S. Wang, L. Yin, and P. He, Grain Refinement and Mechanical Properties Improvement of Inconel 625 Alloy Fabricated by Ultrasonic-Assisted Wire and Arc Additive Manufacturing, *J. Alloys Compd.*, 2022, **910**, p 164957. <https://doi.org/10.1016/j.jallcom.2022.164957>

44. B. Kumar and C. Anandkrishnan, Investigation of the Corrosion Behavior of Wire Arc Additively Manufactured Alloy 825, *Trans. Indian Inst. Met.*, 2022 <https://doi.org/10.1007/s12666-022-02656-9>

Publisher's Note Springer Nature remains neutral with regard to jurisdictional claims in published maps and institutional affiliations.

Springer Nature or its licensor (e.g. a society or other partner) holds exclusive rights to this article under a publishing agreement with the author(s) or other rightsholder(s); author self-archiving of the accepted manuscript version of this article is solely governed by the terms of such publishing agreement and applicable law.